

The stellar populations in the low-luminosity, early-type galaxy NGC 59

A. E. Sansom,^{1★} J. J. Thirlwall,¹ M. A. Deakin,¹ P. Väisänen,^{2,3} A. Y. Kniazev^{2,3,4}
and J. Th. van Loon⁵

¹Jeremiah Horrocks Institute, University of Central Lancashire, Preston PR1 2HE, UK

²South African Astronomical Observatory, PO Box 9 Observatory, 7935, South Africa

³Southern African Large Telescope, PO Box 9 Observatory, 7935, South Africa

⁴Sternberg Astronomical Institute, Lomonosov Moscow State University, Universitetskij Pr. 13, Moscow 119992, Russia

⁵Lennard-Jones Laboratories, Keele University, Staffordshire ST5 5BG, UK

Accepted 2015 March 26. Received 2015 March 18; in original form 2014 September 29

ABSTRACT

Low-luminosity galaxies may be the building blocks of more luminous systems. Southern African Large Telescope observations of the low-luminosity, early-type galaxy NGC 59 are obtained and analysed. These data are used to measure the stellar population parameters in the centre and off-centre regions of this galaxy, in order to uncover its likely star formation history. We find evidence of older stars, in addition to young stars in the emission-line regions. The metallicity of the stellar population is constrained to be $[Z/H] \sim -1.1$ to -1.6 , which is extremely low, even for this low-luminosity galaxy, since it is not classed as a dwarf spheroidal galaxy. The measured $[\alpha/Fe]$ ratio is subsolar, which indicates an extended star formation history in NGC 59. If such objects formed the building blocks of more massive, early-type galaxies, then they must have been gaseous mergers, rather than dry mergers, in order to increase the metals to observed levels in luminous, early-type galaxies.

Key words: galaxies: abundances – galaxies: elliptical and lenticular, cD – galaxies: individual: NGC 59 – galaxies: stellar content.

1 INTRODUCTION

The early-type galaxy NGC 59 is similar in morphology to many other low-luminosity E or S0 galaxies. It has a stellar mass of $\sim 5 \times 10^8 M_{\odot}$. This is about 1/200th of M^* (the knee in the overall galaxy mass function for galaxies in the local Universe), taking $\text{Log}(M^*/M_{\odot}) = 10.64$ from Kelvin et al. (2014). These galaxies form an interesting class of objects whose place in the overall scheme of galaxy evolution has yet to be properly understood.

The hierarchical merger picture of galaxy evolution implies that lower mass galaxies formed before more massive galaxies and that they contributed to the content of more massive galaxies through mergers, over time. Early-type galaxies (ETGs, including elliptical and lenticular) are thought to be particularly affected by this process. Thus, some of the original lower mass galaxies would be consumed in producing giant ellipticals, whilst others, which did not take part in mergers, would still exist today. These ancient relics may look very different today from what they were like at earlier times. For example, at early times they must have contained gas, with which to make new stars, post-merging. This is because the stellar populations of giant galaxies are not the same as those in lower mass galaxies (e.g. Bender, Burstein & Faber 1993; Worthey 1998). In particular, stars in giant galaxies tend to be more metal rich than stars

in lower mass galaxies. This is the well-known mass–metallicity relation, which applies to all types of galaxies (e.g. Gallazzi et al. 2006; Foster et al. 2012). Massive ETGs are also known to have higher $[Mg/Fe]$ ratios than lower mass ETGs (Worthey 1998), or more generally enhanced $[\alpha/Fe]$ element ratios. These are generally interpreted as due to more rapid star formation time-scales in massive ETGs, because of the relative time-scales of different supernova contributions. However alternative explanations have been suggested for varying $[\alpha/Fe]$ ratio, including systematic variations with galaxy mass of the initial stellar mass function or SNIa delay times, or selective wind mass-losses may also affect this ratio (e.g. Pipino et al. 2009).

Lower mass galaxies that survive, without being destroyed in mergers, would continue with their star formation histories (SFHs), unabated. As yet, there have not been many measurements or modelling of abundance patterns from integrated light in ETGs with velocity dispersions below about $\sigma < 80 \text{ km s}^{-1}$. Trends observed at higher velocity dispersions have been well studied (e.g. Graves, Faber & Schiavon 2009; Pipino et al 2009; Conroy, Graves & van Dokkum 2014), showing hints of increased scatter at lower velocity dispersions. More diverse properties at lower mass might be expected from the greater impact of star-forming events on the energetics of systems with smaller gravitational wells (Merlin et al. 2012).

With NTT data, we previously investigated a small sample of nearby, low-luminosity, early-type galaxies (hereafter LLEs;

* E-mail: aesansom@uclan.ac.uk

Sansom & Northeast 2008). The purpose was to compare their stellar populations and kinematics with their more luminous and more massive counterparts (closer to M^* and above) and with similar mass bulges of spiral galaxies. We found that the LLEs fell below extrapolations of trends in metal line strengths, but were consistent with spiral bulges of similar velocity dispersion. Fitted luminosity-weighted mean ages were found to be young (Ages <3 Gyr) and abundances covered a wide range ($-1.4 < [\text{Fe}/\text{H}] < +0.1$), with low $[\alpha/\text{Fe}]$ ratios (typically subsolar). These stellar population characteristics are very different from those of luminous ETGs (e.g. Thomas et al. 2005). The only other galaxies where such characteristics have been detected are in some resolved star data for Local Group dwarf spheroidals (Venn et al. 2004, their fig. 2; Tolstoy, Hill & Tosi 2009), which are much fainter than our original sample of LLEs, and have stellar masses of only a few $\times 10^7 M_\odot$ or less ($<M^*/1000$). The low $[\alpha/\text{Fe}]$ results found for our sample of LLEs have been used to test initial mass functions (IMF) in galaxies, supporting a steeper integrated galactic IMF with increasing galaxy mass and decreasing star formation rate (Recchi, Calura & Kroupa 2009). LLEs provide important tests of scaling relations with mass and luminosity in general, since they are at one extreme of those relations.

A few other studies have measured detailed stellar population parameters in LLEs, including that of Annibaldi et al. (2011), who studied a small sample of ETGs with M_R in the range -19.8 to -14.8 . They found generally subsolar metallicities and subsolar $[\alpha/\text{Fe}]$ on average, with some hints of environmental dependences, when comparing their ETGs in poor groups with results from the Coma cluster. Koleva et al. (2013, and references therein) measured stellar population age and $[\text{Fe}/\text{H}]$ in samples of dwarf ETGs and transition-type dwarfs, covering $M_B = -19.0$ to -14.5 and found a wide range of, typically subsolar metallicities, around -0.7 dex on average, from their luminosity-weighted, simple stellar populations (SSP) fits.

The signal to noise in LLE spectra is generally not as high as for many luminous ETGs that have been the subject of stellar population analysis. Therefore, results for LLEs may be more susceptible to the well-known age–metallicity degeneracies that plague such analysis. It is for this reason that we wished to check our results for the most extreme LLEs, using new data that is more sensitive to stellar population parameters. From our NTT data, we found that the S0 galaxy NGC 59 ($M_B = -15.57$) had central stellar velocity dispersion of $37 \pm 5 \text{ km s}^{-1}$ and the following stellar population parameter estimates: Age = 1.5 ± 0.1 Gyr, $[\text{Fe}/\text{H}] = -1.350 \pm 0.075$ and $[\alpha/\text{Fe}] = -0.300 \pm 0.075$ dex. Whilst other LLEs that we observed also had similarly unusual stellar populations, NGC 59 was the most extreme. Therefore, in this paper we test the results for this galaxy with new data, taken with the SALT (O’Donoghue et al. 2006), covering a wavelength range extending further into the blue region and using stellar population models, based on state-of-the-art stellar spectral libraries.

NGC 59 is classified as SA0 in RC3 (de Vaucouleurs et al. 1991) and E in the APM Bright Galaxy Catalogue (Loveday 1996). It is usually classified as a dwarf, ETG. Bouchard et al. (2005) reclassified this galaxy to a dS0 Pec on the basis of its H I and $\text{H}\alpha$ detections. Beaulieu et al. (2006) measured $\text{H I} = 1.4 \pm 0.1 \times 10^7 M_\odot$ in NGC 59 and suggest that this H I mass and $m(\text{H I})/L_B$ ratio are closer to those of dIrr and normal spiral galaxies than dEs. Star formation activity was detected by Skillman, Côté & Miller (2003), in which the $\text{H}\alpha$ image shows lumpy, approximately central $\text{H}\alpha$ emission (their fig. 1). Images in several wavebands are also shown in Saviane et al. (2008, their fig. 1). The nucleus of NGC 59 was resolved in J , H and K images, revealing two peaks ≈ 2.3 arcsec apart (de Swardt, Kraan-Korteweg & Jerjen 2010, their fig. 3), with the

northern component assumed to be the true stellar nucleus and the southern component a star-forming region. De Swardt et al. (2010) also estimated the total stellar mass of NGC 59 to be $5 \pm 2 \times 10^8 M_\odot$, from their H -band data. NGC 59 is nearby, at a distance of only 4.4 Mpc and it is part of the Sculptor group of galaxies. The proximity and unusual stellar population in NGC 59 make it an interesting early-type dwarf galaxy to study. More observations of ETGs in this low mass regime will help to constrain models of galaxy formation.

The observations are described in Section 2, and then the data reductions are presented in Section 3, including kinematics and emission-line strengths. Absorption lines are measured in Section 4 and stellar population analysis is presented in Section 5. Section 6 gives the conclusions.

2 SALT OBSERVATIONS

SALT is an 11-m optical telescope that is optimized to be efficient in the blue region of the spectrum, thanks to its optical design and coatings. We used the Robert Stobie Spectrograph (RSS) on SALT to obtain medium resolution spectra across a broad wavelength range (Burgh et al. 2003, Buckley et al. 2008). For the extreme blue part of the spectrum, we used the PG3000 grating, covering 3440–4220 Å, with slit width 0.6 arcsec, giving a resolution of 1.18 \AA ($0.26 \text{ \AA pixel}^{-1}$). For redder wavelengths, we used the PG1300 grating, covering 3990–6080 Å, with slit width 1.25 arcsec, giving a resolution of 2.20 \AA ($0.67 \text{ \AA pixel}^{-1}$). For both the blue and red spectra, the binning was a factor of 2 in the spectral direction and a factor of 4 in the spatial direction, giving 0.5068 arcsec per spatial bin along the slit. The data were observed between 24/05/2012 and 11/10/2012, including 3×800 plus 1100 s in the blue and 3×900 s in the red, plus observations of three Lick standard stars in both blue and red spectral modes. All observations were performed in seeing conditions between 2 and 3 arcsec. The slit position was along the minor axis of NGC 59, at PA = 37° east of north (or 180° around from there), for all spectra except for one of the PG3000 spectra which had PA = 65° . These latter data were included to increase the signal to noise in the blue. Fig. 1 shows a red Digitized Sky Survey (DSS) image of the galaxy with the slit positions overlaid. The inset is a zoom-in of the nucleus on our short 3-s RSS acquisition image in white light. In poor seeing conditions a north–south elongation of the nucleus is just detectable, corresponding to the direction of the second nucleus apparent in fig. 3 of de Swardt et al. (2010).

The detector consists of three adjacent CCDs with two gaps. We chose wavelength ranges so as to minimize the loss of important regions of the spectra. Thus, the blue spectrum covers higher order Balmer lines from $\text{H}\delta$ and above, plus the Ca H&K features, whilst the red spectrum covers from $\text{H}\delta$ up to the NaD doublet. This then includes most of the standard Lick spectral indices, which are extensively used in stellar population analysis (Worthey 1994; Proctor & Sansom 2002; Johansson, Thomas & Maraston 2012), plus higher order Balmer lines, which are sensitive to the age of the most recent star formation (Worthey & Ottaviani 1997).

3 DATA REDUCTIONS

3.1 Basic reductions

The preliminary reduced data obtained from the SALT pipeline (Crawford et al. 2010) were further reduced in IRAF. We divided by an illumination flat and wavelength calibrated the spectra, giving a typical uncertainty of $\pm 0.06 \text{ \AA}$ in the blue and $\pm 0.18 \text{ \AA}$ in the

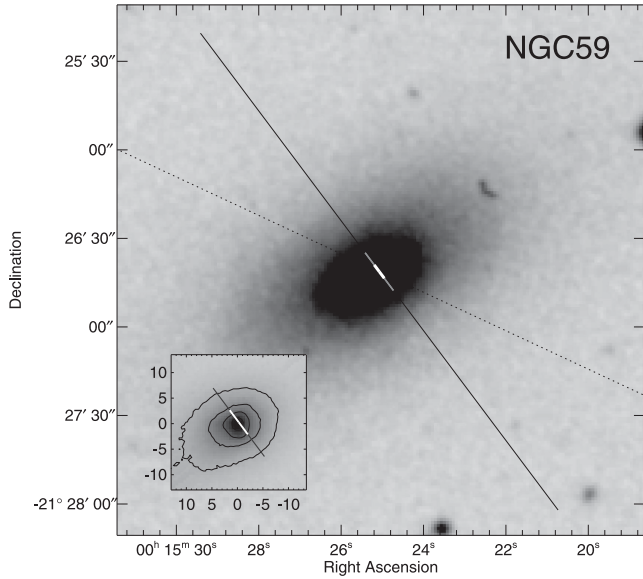


Figure 1. A 3 arcmin \times 3 arcmin photographic red DSS image of NGC 59, north is up, east to the left. The main RSS slit orientation PA = 37° is overlaid on the image with a solid line, and the extracted apertures indicated the white part of the line is the Central region, and the grey sections of the line indicate the lower (south west) and upper (north-east) apertures discussed in the text (Section 3.1). The PA = 60° slit is shown as the dotted line. The inset shows the nuclear area from the RSS acquisition image with clear filter, where some photometric asymmetry is evident. The inset tick marks are in arcsec.

red. At the centres of these two spectral ranges, this corresponds to velocity uncertainties of 4.7 and 10.7 km s⁻¹, respectively. The 2-d data were cosmic ray cleaned using *xzap* in IRAF and the spectra were background subtracted using a second-order polynomial. A relative flux calibration was carried out using flux standard star EG21, from observations taken as close in time as possible to the galaxy observations. This was done with a spline fit, order 6 applied to the flux standard data. The galaxy spectra were then combined using *lscombine*, with additional cosmic ray cleaning, to give two cleaned, summed spectra, one in the blue and one in the red, with a total exposure of 3500 s in the blue spectrum and 2700 s in the red spectrum for the target galaxy.

A few cosmic ray features remained in the 2-d spectral images, despite efforts to clean them automatically in the processing above. Therefore, we also carried out a final visual check of the spectral images and patched out any remaining cosmic ray effects that we could identify. This does not preclude the presence of faint cosmic rays, which would go unnoticed against the background of rapidly changing light across the spectral images for NGC 59.

Error arrays for the galaxy observations were generated initially from the counts in the original 2-d data files, and errors were propagated at each step in the data reductions. The resultant random error arrays highlight where the noise is highest (e.g. due to strong sky lines, emission lines in the galaxy and increasingly towards the blue end of the PG3000 grating spectrum. These arrays were used in the subsequent analysis, including determination of signal-to-noise ratios (S/N).

Spectra were extracted for the three Lick calibration stars, which are also velocity standard stars, for the flux calibration stars and for the galaxy observations, in each of the blue and red spectral modes. The spectra for Lick stars and for the galaxy were flux calibrated using the standard star data. This is a relative flux calibration only,

since absolute flux calibration is difficult with SALT and weather conditions cannot be assumed to be photometric.

Three spatial regions in NGC 59 were measured.

(i) Central region covers $r_e/8$ either side of centre, which is 11 spatial pixels across (5.6 arcsec), taking r_e as 21.73 arcsec from RC3.

(ii) Upper region covers 10 spatial pixels above the central region (5.1 arcsec).

(iii) Lower region covers 10 spatial pixels below the central region (5.1 arcsec).

The central spatial region corresponding to a radial extent of $r_e/8$ (~ 11 pixels in diameter) has a typical S/N ≈ 47 in the blue spectrum and S/N ≈ 60 in the red spectrum, ignoring the blue regions (below ~ 3800 Å, where the S/N drops rapidly).

3.2 Kinematics and emission lines

The Lick standard stars were first analysed in order to align them to a rest wavelength scale. The spectra were cross-correlated to determine their relative spectral shifts. The heliocentric velocity of one template star was found from the SIMBAD data base and used to determine observed shifts for all the Lick standard stars. Once these shifts were known *dopcor* and *dispcor* in IRAF were used to correct and resample the star spectra to a rest wavelength scale, with the same range and sampling as for the galaxy data. The aligned Lick star spectra could be used as templates for measuring galaxy kinematics, since the stars and galaxy were observed with the same setup. The penalized pixel fitting *PPXF* software (Cappellari & Emsellem 2004) was used to measure kinematics for NGC 59, using the PG1300 data only. Emission lines, gap regions, residual sky lines and edges were masked out for these measurements. This gave a first velocity dispersion estimate of 27 ± 11 km s⁻¹ and a measured recession velocity of 332 ± 9 km s⁻¹.

Since there were only three Lick standard stars observed, the template match to NGC 59 was not very accurate. To improve the accuracy of template stars to describe the absorption line spectrum in NGC 59, template spectra of SSPs based on stars in the MILES spectral library from 2006 were used (Sarzi private communication). To use the MILES spectra, the SALT spectra were Gaussian blurred to the same spectral resolution of 2.5 Å FWHM (Falcón-Barroso et al. 2011). Running the *PPXF* software on these blurred SALT data for NGC 59, with the MILES SSPs as templates led to the second velocity dispersion estimate of 47 ± 23 km s⁻¹.

Both of these estimates are similar to our previous estimate of 37 ± 5 km s⁻¹, using data from the NTT with a large sample of Lick standard stars (Sansom & Northeast 2008). For the rest of this paper, we use this previous estimate of velocity dispersion, since it was obtained using more kinematic standard stars, giving a better template match to the galaxy at the resolution of those observations.

In order to measure emission lines, the two SALT gratings (PG3000 and PG1300) were first combined, from the same spatial region as far as possible, in the following way. Both the spectra were resampled on to the full spectral range (3440.6–6080.0 Å) at the binning of the PG1300 spectra, then the overlap region (3990.0–4219.8 Å) was normalized to the PG1300 value, halved, added together with the shorter and longer wavelength data from single grating observations. This led to a spectrum that was well matched across the two grating observations. This spectrum was then blurred to the resolution of MILES, so that the full range of MILES SSP spectra could be used as templates during the emission-line measurements. The spectrum of NGC 59 was also binned to the

Table 1. Emission-line measurements relative to H β . The relative intensities are measured from NGC 59 after continuum model subtraction, using programs described in Kniazev et al. (2004, 2005). Note that the derived Balmer absorption EW(abs) ≈ 0 indicates the absorption was correct in the continuum model (see text). Extinction is derived from a simultaneous iterative fit to the emission-line intensities, absorption characteristics and temperature information using the direct method with the [O III] λ 4363 Auroral line. All relevant errors have been propagated to the uncertainties including those from the continuum fitting.

$\lambda_0(\text{\AA})$ Ion	$F(\lambda)/F(\text{H}\beta)$ (measured)	$I(\lambda)/I(\text{H}\beta)$ (corrected)
3727 [O II]	1.8667 \pm 0.0857	2.2846 \pm 0.1089
3771 H11	0.0140 \pm 0.0040	0.0170 \pm 0.0070
3798 H10	0.0214 \pm 0.0034	0.0259 \pm 0.0065
3835 H9	0.0513 \pm 0.0032	0.0614 \pm 0.0061
3868 [Ne III]	0.4282 \pm 0.0095	0.5094 \pm 0.0125
3889 He I + H8	0.1847 \pm 0.0049	0.2189 \pm 0.0079
3967 [Ne III] + H7	0.2315 \pm 0.0103	0.2702 \pm 0.0133
4026 He I	0.0146 \pm 0.0011	0.0169 \pm 0.0012
4068 [S II]	0.0227 \pm 0.0026	0.0260 \pm 0.0030
4076 [S II]	0.0041 \pm 0.0009	0.0047 \pm 0.0011
4101 H δ	0.2550 \pm 0.0058	0.2902 \pm 0.0083
4340 H γ	0.4220 \pm 0.0094	0.4600 \pm 0.0112
4363 [O III]	0.0492 \pm 0.0017	0.0535 \pm 0.0019
4471 He I	0.0297 \pm 0.0017	0.0317 \pm 0.0018
4861 H β	1.0000 \pm 0.0294	1.0000 \pm 0.0297
4922 He I	0.0081 \pm 0.0011	0.0081 \pm 0.0011
4959 [O III]	1.5665 \pm 0.0335	1.5432 \pm 0.0332
5007 [O III]	4.7950 \pm 0.1026	4.6896 \pm 0.1009
5518 [Cl III]	0.0046 \pm 0.0011	0.0042 \pm 0.0010
5538 [Cl III]	0.0028 \pm 0.0008	0.0025 \pm 0.0007
5876 He I	0.1212 \pm 0.0029	0.1054 \pm 0.0027
$C(\text{H}\beta)$ dex		0.28 \pm 0.04
$E(B - V)$ mag		0.19 \pm 0.03
A_V mag		0.59 \pm 0.08
EW(abs) \AA		0.00 \pm 0.13
EW(H β) \AA		44 \pm 1

MILES sampling of 0.9 \AA pixel $^{-1}$. A best-fitting template spectrum (Best_Template), combining several SSPs, was obtained by running PPF with the emission lines masked out. The Best_Template was output as a spectrum, with Galactic extinction incorporated to match the observations, assuming Calzetti et al. (2000) reddening plus Galactic $E(B - V) = 0.019$ mag, from NED.¹

Emission lines in the spectrum of NGC 59 were then accurately measured, making use of the Best_Template and applying programs described in detail in Kniazev et al. (2004, 2005). Table 1 lists the measured relative intensities of all detected emission lines relative to H β ($F(\lambda)/F(\text{H}\beta)$) and the ratios corrected for the extinction ($I(\lambda)/I(\text{H}\beta)$). The equivalent width (EW) of the H β emission is also listed as is the derived extinction coefficient $C(\text{H}\beta)$. The latter is a sum of the internal extinction in NGC 59 and foreground extinction in the Milky Way. The measured $C(\text{H}\beta)$ corresponds to a V-band extinction of $A_V = 0.59$ mag. Accounting for the Milky Way foreground extinction of 0.06 mag (Schlegel, Finkbeiner & Davis 1998), this suggests non-negligible dust content of $A_V \sim 0.5$ mag extinction in the central H II region of NGC 59.

Our emission-line measurement programs determine the location of the continuum, perform a robust noise estimation and fit separate lines by a single Gaussian superimposed on the continuum-

Table 2. Elemental abundances in NGC 59.

$T_e(\text{O III})(\text{K})$	12 139 \pm 173
$T_e(\text{O II})(\text{K})$	11 952 \pm 149
$N_e(\text{O II})(\text{cm}^{-3})$	48 \pm 33
$\text{O}^+/\text{H}^+(\times 10^5)$	4.477 \pm 0.297
$\text{O}^{++}/\text{H}^+(\times 10^5)$	9.161 \pm 0.418
$\text{O}/\text{H}(\times 10^5)$	13.640 \pm 0.513
12+log(O/H)	8.13 \pm 0.03
$\text{Ne}^{++}/\text{H}^+(\times 10^5)$	2.678 \pm 0.149
ICF(Ne)	1.141
$\text{Ne}/\text{H}(\times 10^5)$	3.06 \pm 0.17
12+log(Ne/H)	7.49 \pm 0.02
log(Ne/O)	-0.65 \pm 0.03
$\text{Cl}^{++}/\text{H}^+(\times 10^7)$	0.291 \pm 0.056
ICF(Cl)	1.286
$\text{Cl}/\text{H}(\times 10^7)$	0.37 \pm 0.07
12+log(Cl/H)	4.57 \pm 0.08
log(Cl/O)	-3.56 \pm 0.08

subtracted spectrum (Kniazev et al. 2004). In this particular case, since a best-fitting model was already created, the model was used as the continuum. The quoted errors of single line intensities include components summed up in quadrature (Kniazev et al. 2004). The total errors were propagated in the calculations and are included in the uncertainties of the element abundances and all other derived parameters presented here. Note that our programs are designed to derive simultaneously both the extinction coefficient $C(\text{H}\beta)$ and the absorption equivalent width $\text{EW}_{\text{abs}}(\lambda)$ for the hydrogen lines as described in Izotov, Thuan & Lipovetsky (1994). We can use this to check the consistency between the model continuum and the emission lines. The result for absorption lines is $\text{EW}_{\text{abs}}(\lambda) = 0.00 \pm 0.13$ \AA which means that the model that was subtracted describes very well the Balmer absorption since no additional component is needed to explain the emission-line ratios beyond extinction. We experimented with slightly different models as well, and also by forcing $\text{EW}_{\text{abs}}(\lambda) = 0$, and the results for all emission-line parameters stay the same within the uncertainties, which also stay the same. We note that the uncertainty of 0.13 for the Balmer absorption is propagated through all the results, and, in fact, is very similar to the uncertainty of the Balmer line Lick indices derived below by very different and independent methods.

The H II region spectrum was interpreted by the technique of plasma diagnostics and iterative calculations as described in detail in Kniazev et al. (2008). The results regarding temperatures, the number density n_e derived using the [O II] λ 3726/ λ 3729 lines ratio and the total elemental abundances for O, Ne and Cl, are given in Table 2. The electron temperature $T_e(\text{O III})$ was calculated directly using the weak auroral line of oxygen [O III] λ 4363.

The relative emission-line intensities given in Table 1 are consistent with a star-forming origin, considering the location of [O II]/H β versus [O II]/[O III] in the line ratio diagrams like those of Baldwin, Phillips & Terlevich (1981), their fig. 2. This is consistent with the findings of previous authors. Skillman et al. (2003) mapped and analysed the H α emission in NGC 59. From H α emission and GALEX FUV fluxes, Karachentsev & Kaisina 2013 estimated star formation rates of $\text{SFR}_{\text{H}\alpha} = 0.0123 M_{\odot} \text{yr}^{-1}$ and $\text{SFR}_{\text{FUV}} = 0.0063 M_{\odot} \text{yr}^{-1}$, respectively, which agree quite well within their expected uncertainty of ~ 50 per cent, confirming the star-forming origin of the emission lines. Bouchard et al. (2005) suggested that NGC 59 be reclassified as dS0 Pec, due to the detection of neutral and ionized components near the centre. All the

¹ NED is the Nasa Extragalactic Database at <http://ned.ipac.caltech.edu>

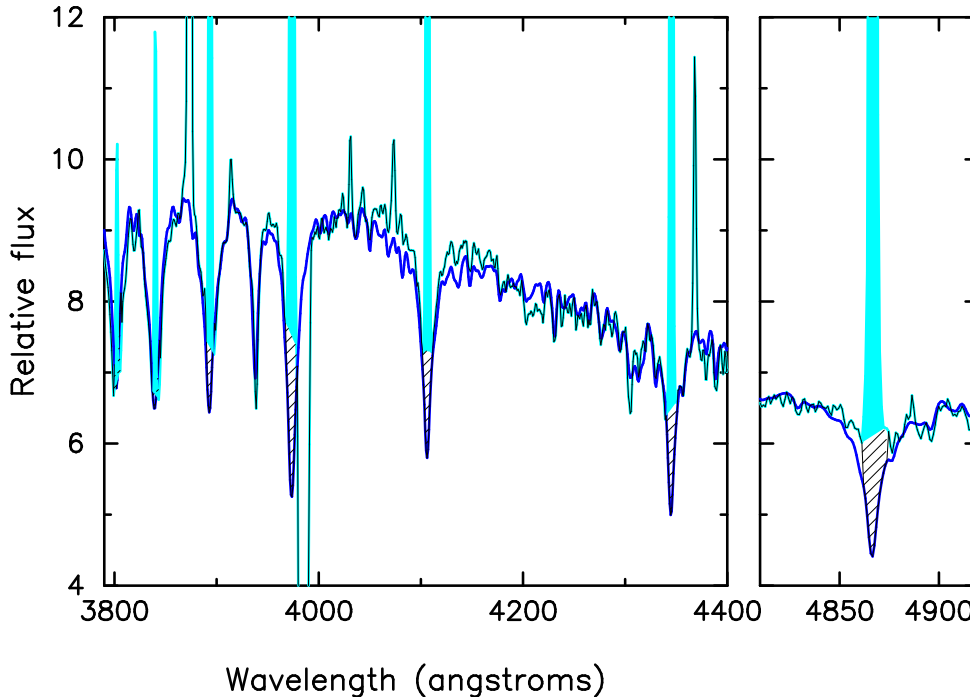


Figure 2. Balmer line regions in the central spectrum in NGC 59, illustrating the replacement of the cores of Balmer lines, where strong emission lines originally dominated those data. The thick cyan lines are the original spectral data, the thick dark blue lines are the best-fitting MILES template data and the thin black lines are the Balmer line core-corrected spectral data. Other emission lines are subsequently removed by interpolation across them, to produce the lower spectrum shown in Fig. 3.

reddening-corrected Balmer lines measured here (Table 1), including the well-determined higher order lines (H9 to H11), show ratios that are consistent with expectations for hydrogen recombination lines from a typical H II region (e.g. Skillman et al. 1994).

Abundances in the gas were estimated from the observed emission lines, using the software of Kniazev, with the direct method because the [O III] line at 4363 Å is detected. The oxygen abundance $12+\log(\text{O}/\text{H}) = 8.13 \pm 0.03$ dex (i.e. $\sim 1/5$ solar, e.g. compared to Grevesse & Sauval 1998) that we find for NGC 59 is reasonably consistent with the abundance 8.29 ± 0.08 dex published by Saviane et al. (2008). Our data also allow us, for the first time, to determine abundances of Ne and Cl in NGC 59, which are also approximately $1/5$ solar to within about 20 per cent. It is known that H II region abundances mainly provide information about α -process elements, which are produced predominantly in short-lived massive stars. The relative abundances of $\log(\text{Ne}/\text{O})$ and $\log(\text{Cl}/\text{O})$ in Table 1 are consistent with values for a large sample of H II regions in blue compact galaxies Izotov & Thuan (1999) and a large sample of H II galaxies (Izotov et al. 2006) from the Sloan Digital Sky Survey DR3 data (Abazajian et al. 2005).

3.3 Removing emission lines

Subtracting the emission lines proved difficult to do accurately, since emission lines near the centre of NGC 59 are quite strong and their spectral shape in the SALT data did not appear to follow a Gaussian accurately enough to subtract them well using *gandalf* (Sarzi et al. 2006). An alternative solution was used to remove the estimated contributions from emission lines. For all hydrogen Balmer lines in the spectral range, core regions (width ~ 10 Å) affected by emission were replaced by data from Best_Template, as our best estimate of the shape and strength of the hydrogen absorption line cores.

This is illustrated in Fig. 2, which shows a closeup of the Balmer line regions, illustrating the original data (thick cyan line), the best-fitting template (thick dark blue line) and the data with Balmer cores replaced (thin black line). For other emission lines, simple interpolation across the lines was applied and these regions flagged for subsequent information. Fig. 3 shows the original central spectrum (top plot), and then the final central spectrum with the hydrogen line emission replaced and other emission lines removed (lower plot). Although we are replacing part of the hydrogen lines by template data, rather than real data for NGC 59, this produces more realistic hydrogen absorption line shapes than subtracting the emission lines using *gandalf*. This replacement process was thought to be the best compromise, given that the core absorption line data is lost due to the strong emission lines. H7 at 3970 Å is lost in one of the gaps, but many other Balmer lines are clearly visible. The consistency of measured higher order Balmer line emissions (shown in Table 1) helps to support the validity of our approach. Higher order Balmer absorption lines are less affected by emission-line contamination.

At short wavelengths, there is a hint of UV upturn in the spectrum (Kaviraj et al. 2007); however, near the blue edge of the data, below ~ 3500 Å the flux calibration becomes unreliable.

4 ABSORPTION LINE MEASUREMENTS

Standard Lick absorption lines were measured using the LECTOR software available from <http://miles.iac.es/pages/software.php>. Perturbations applying the error arrays were used to generate 500 Monte Carlo realizations of the data, from which random errors were estimated for the line-strength measurements. Line-strength errors due to uncertainties in kinematics (velocity and velocity dispersion) were evaluated by varying the assumed kinematic within their estimated errors and remeasuring the line strengths. These uncertainties

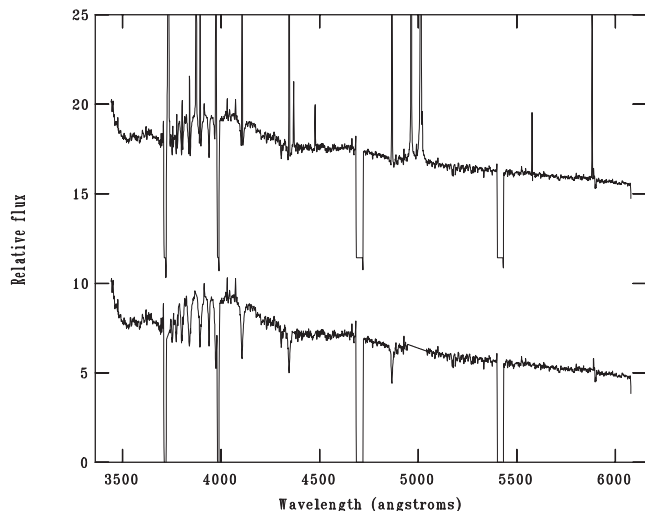


Figure 3. Central spectrum in NGC 59. This plot shows the processing to remove emission lines from the spectrum. Data were taken with the SALT in two grating settings, combined as described in the text. The top plot is offset vertically and shows the combined data before attempting to remove any emission-line features. This shows four gap regions, two associated with each grating observation, centred around 3716 and 3985 Å in the blue, and around 4703 and 5417 Å in the red. Emission lines are strong and the hydrogen Balmer series shows both emission lines and broader absorption line components. Residual sky line features are apparent at 5577 Å and residual contamination due to strong cosmic rays affects the NaD doublet such that we do not use it in our subsequent analysis in Section 5. The lower plot shows the same spectrum with the Balmer emission-line regions replaced by data from the best-fitting MILES SSP template and several strong emission lines removed by interpolating across those regions.

were found to be significantly less than the random errors. Uncertainties in the Balmer line cores were estimated by trying fits using different parts of the spectrum, but still including all the Balmer lines, including removing the continuum regions above $H\beta$ and below the Balmer limit. This led to estimated Balmer line errors from our core H line replacement procedure. All these errors were added together in quadrature to give total estimated errors for each index. Two Lick features were lost due to partially falling within gap regions (C₂4668 and Fe5406). Another Lick feature was lost due to falling too close to strong emission lines (Fe5015). The data and error estimates are given in Table 3, for the three regions measured in NGC 59.

Fig. 4 shows a plot of these three regions. Evidence of young stars is present in all three spectra, from the strength of the Balmer absorption lines. From the cleaned spectra in Figs 3 and 4, it is already possible to see that this is a low-metallicity galaxy, from the weakness of the metal-sensitive lines around Mg_b. One possibility to consider for NGC 59 is that nebular continuum emission may decrease its apparent absorption line strengths. Reines et al. (2010) studied relative contributions to continuum emission from stars and gas in young massive star clusters. For example, their fig. 8 shows that if all the stars had formed only 5 Myr ago, then the nebular continuum is only 5 per cent of the total continuum. The results presented here (e.g. Fig. 3), including strong Balmer absorption lines in NGC 59, show that stars older than 5 Myr dominate the light. This is also supported by full spectrum fitting described below in Section 5.4. Therefore, the effect of nebular continuum emission is unlikely to cause a significant bias for the Lick absorption line measurements in NGC 59.

The upper, off-centre region extends beyond the two peaks of near-infrared emission mapped by de Swardt et al. (2010), which they assumed to be associated with the centre of the galaxy and a star-forming peak 2.3 arcsec to the south. Therefore, it is interesting to see if different stellar population characteristics are uncovered in these regions beyond the central star-forming area, perhaps better characterizing the bulk of stars in NGC 59.

Table 3 shows how the spectra change between central and off-centre regions, with hydrogen absorption lines becoming generally weaker in the lower region. There is an anomalously weak measurement of Fe5270 in the lower region, which is investigated below. These data are used to characterize the stellar populations in the next section.

5 STELLAR POPULATION ANALYSIS

5.1 Lick system – MILES SSPs

The indices from Table 3, at the standard Lick resolutions (Worthey & Ottaviani 1997), were used to estimate luminosity-weighted average SSP age, metallicity and $[\alpha/\text{Fe}]$ across NGC 59. This uses software written by R. Proctor, based on the SSP results of Korn, Maraston & Thomas 2005, plus references therein. CN1 was excluded from these fits since it is too strongly affected by $H\delta$ in its blue side band. Results are given in Table 4.

The fit for the lower region led to an old age, qualitatively inconsistent with the presence of emission lines in this spectrum, suggesting some more recent or ongoing star formation. The initial fit was quite poor due to an anomalously low value of Fe5270, which when removed led to a significant improvement in chi-squared at similar parameters. On further inspection, a small peak in the lower spectrum, in the central band of Fe5270 adversely affects this measurement and appears to correspond to a possible weak cosmic ray event in one of the original images. We note that removing a remaining outlier, the Mg1 index, leads to a younger estimated age ($\text{Log}(\text{Age}) = 0.8$ dex) while the metallicity remains low and the abundance ratio subsolar. This gives an indication of the parameter uncertainties due to the inclusion or exclusion of specific indices. The fit with Fe5270 removed is shown in Table 4. For this low metallicity ($[Z/H] \sim -1.6$), the SSP line strengths change little with age, for ages greater than 8 Gyr (see Fig. 5) and the Balmer line strengths start to vary non-monotonically. Therefore, the best-fitting SSP age of this lower region is difficult to constrain beyond saying that it is older than ~ 8 Gyr. The uncertainty in age estimate given for this lower region in Table 4 is an underestimate since we can only give this lower limit to the age. Therefore, we do find evidence of older stars ($> \sim 8$ Gyr) in NGC 59, beyond the central, strongest emission-line region. Jerjen, Binggeli & Freeman (2000) studied its optical brightness profile and colours and found a Sérsic index of $n = 0.63$ in B, with $B - R$ colour becoming redder further out, indicative of older stars.

The centre region was not well fitted by a single SSP ($\chi_r^2 = 2.63$). Outlying indices were removed to see what effect this would have on the fit and derived parameters. Removing two indices (Mg1 and Fe5270) brought the χ_r^2 down to 1.4, but did not significantly alter the derived parameter values. Therefore, we show the fit including those three indices in Table 4. In Section 5.3 below, we make a preliminary search to see if two SSPs will better describe this central region of NGC 59. The metallicity of the centre region is similar to that in the lower region. The low $[\text{Fe}/\text{H}]$ abundance found in the centre of NGC 59 is also supported by the Rose indices measured using LECTOR in this region. For NGC 59, we measured

Table 3. NGC 59 line strengths measured at MILES resolution (FWHM = 2.5 Å), for standard Lick band definitions. Standard deviations (SD) are 1 sigma random errors derived from 500 realizations of the spectra, perturbed by the error array. Dsig errors are derived by accounting for the uncertainty in velocity dispersion estimated from the current data. Similarly, Dvel errors are derived by measuring the changes in indices considering the uncertainty in recession velocity. H errors are estimated uncertainties in the Balmer line core replacement. Total errors add all these error sources together, in quadrature. The errors are dominated by the random errors and by Balmer line core uncertainties. The mask values are '1' for good indices, included in later fits, and '0' for indices with problems, excluded from later fits. These latter indices include C₂4668 and Fe5406, which fall into the gap regions between CCDs; Fe5015, which overlaps regions containing strong emission lines. The line strengths for these three indices are not shown here. This mask array applies to all three spatial regions, unless otherwise stated in the text. Also tabulated are results for the same three regions, at the Lick standard resolution (from Worthey & Ottaviani 1997) at FWHM ~8.4–10.9 Å.

Name:	H δ _A	H δ _F	CN1	CN2	Ca4227	G4300	H γ _A	H γ _F	Fe4383	Ca4455	Fe4531	H β	Mg1	Mg2	Mgb	Fe5270	Fe5335	Fe5709	Fe5782
<i>Central (r_e/8) region. MILES resolution</i>																			
Value:	4.856	3.977	-0.098	-0.051	0.176	0.475	3.254	3.132	0.578	0.395	1.286	3.103	0.020	0.041	0.962	0.657	0.688	0.473	0.287
SD err:	0.163	0.116	0.005	0.006	0.092	0.168	0.176	0.124	0.261	0.121	0.180	0.170	0.003	0.003	0.126	0.144	0.153	0.103	0.102
Dsig err:	0.003	-0.003	0.000	0.000	-0.001	0.000	-0.002	-0.014	-0.052	0.016	-0.006	0.003	-0.001	-0.001	-0.007	-0.003	-0.008	-0.001	0.005
Dvel err:	0.000	0.003	0.000	-0.001	0.005	-0.026	0.001	0.002	-0.003	-0.008	-0.005	-0.000	0.000	-0.000	0.009	-0.007	-0.016	0.003	-0.004
H err:	0.638	0.643				0.428	0.428					0.499							
Total err:	0.658	0.653	0.005	0.006	0.092	0.170	0.463	0.446	0.266	0.122	0.180	0.527	0.003	0.003	0.126	0.145	0.154	0.103	0.102
Mask:	1	1	0	1	1	1	1	1	1	1	1	1	1	1	1	1	1	1	1
<i>Upper region. MILES resolution</i>																			
Value:	4.636	4.013	-0.124	-0.081	0.948	1.469	2.601	3.458	2.468	0.226	1.445	3.488	0.025	0.074	1.227	1.890	1.282	0.483	0.391
Total err:	0.761	0.735	0.010	0.012	0.185	0.357	0.463	0.553	0.507	0.233	0.378	0.484	0.005	0.006	0.241	0.274	0.297	0.187	0.193
<i>Lower region. MILES resolution</i>																			
Value:	4.143	3.527	-0.077	-0.026	0.434	1.162	2.344	3.167	1.850	-0.212	1.439	2.436	0.032	0.063	0.919	0.457	0.732	0.638	0.177
Total err:	0.719	0.684	0.010	0.012	0.173	0.329	0.375	0.656	0.441	0.232	0.346	0.408	0.005	0.005	0.196	0.228	0.251	0.141	0.141
<i>Central (r_e/8) region. Lick Standard resolution</i>																			
Value:	4.815	3.644	-0.097	-0.065	0.084	0.290	3.194	2.899	0.468	0.267	1.088	2.996	0.020	0.041	0.830	0.558	0.568	0.435	0.274
Total err:	0.658	0.653	0.005	0.006	0.095	0.171	0.463	0.443	0.277	0.124	0.200	0.526	0.003	0.003	0.127	0.139	0.158	0.103	0.100
<i>Upper region. Lick Standard resolution</i>																			
Value:	4.670	3.636	-0.127	-0.099	0.667	1.128	2.617	3.215	2.298	0.056	1.369	3.409	0.025	0.073	1.029	1.747	1.057	0.484	0.297
Total err:	0.713	0.736	0.010	0.012	0.191	0.350	0.455	0.549	0.490	0.236	0.396	0.481	0.006	0.006	0.242	0.241	0.301	0.201	0.179
<i>Lower region. Lick Standard resolution</i>																			
Value:	4.163	3.210	-0.079	-0.044	0.261	0.926	2.275	2.911	1.669	-0.168	1.246	2.493	0.031	0.062	0.871	0.371	0.610	0.516	0.187
Total err:	0.723	0.685	0.010	0.012	0.178	0.333	0.360	0.650	0.479	0.228	0.357	0.411	0.004	0.005	0.186	0.219	0.235	0.139	0.137

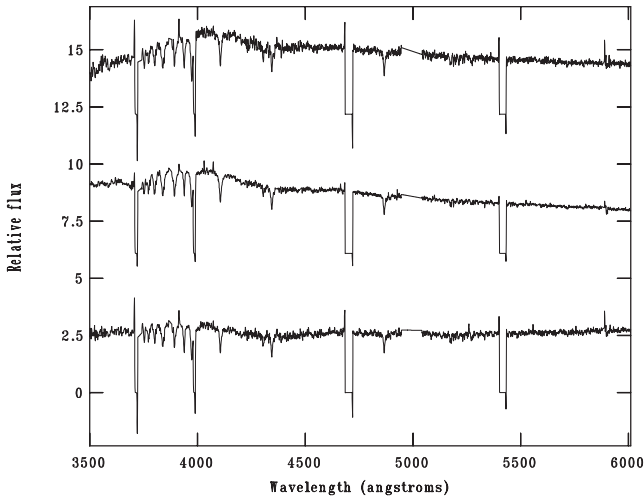


Figure 4. From bottom to top, this plot shows cleaned spectra of the lower, central and upper regions in NGC 59, with vertical offsets to separate the plots. The central region is the same as in the lowest plot in Fig. 3. All three spectra have had the cores of their hydrogen Balmer lines replaced by the best-fitting SSP template from the MILES SSP data base, in order to remove the emission-line contamination from those lines. Other strong emission lines have been removed by interpolating across them.

$H\delta/FeI\lambda 4045 = 0.654$ and $FeI\lambda 4045/FeI\lambda 4063 = 1.012$, which implies $[Fe/H] \sim -1.5$ (Rose et al. 1994, their fig. 10). The centre region has a fitted SSP age of ~ 5 Gyr.

The upper region is adequately fit by a single SSP ($\chi_r^2 = 1.4$), which is relatively young (3.5 Gyr). The upper region is fit by the highest overall metallicity ($[Z/H] \sim -1.05$), which is still low amongst ETGs. The best-fitting $[\alpha/Fe]$ ratio is subsolar in all regions, similar to what we found previously with the NTT data (Sansom & Northeast 2008), where only one spectrum was analysed.

In general, the ages and abundance ratios are not very well constrained by these data. However, the very low metallicity in NGC 59 ($[Z/H] < 1/10$ th of solar) is a more robust result. These results are illustrated in the index–index plots of specific features shown in Fig. 5, where the locations and uncertainties of the three regions in NGC 59 are plotted against grids of MILES SSP predictions.

5.2 Lick system – EZ_AGES

The above results were tested using an alternative stellar library and fitting software called EZ_AGES (Graves & Schiavon 2008), downloaded from http://astro.berkeley.edu/~graves/ez_ages.html. This code uses SSPs based on the Jones and INDO-US stellar libraries, as described in Schiavon (2007) and fits to Lick standard indices.

Briefly, at solar abundance pattern, the ages searched are 1.2, 1.5, 2.5, 2.8, 3.5, 5.0, 7.0, 10.0 and 14.1 Gyr, and the $[Fe/H]$ values searched are -1.3 , -0.7 , -0.4 , 0.0 and $+0.2$ dex. EZ_AGES could not be used to fit indices for NGC 59 in the central and lower regions because this galaxy has a very low metallicity, falling below the lowest predictions, at $[Fe/H] = -1.3$, in EZ_AGES. This is illustrated in the output index–index plots, an example of which is shown in Fig. 6. Lines of constant $[Fe/H]$ (solid lines) are shown, with $[Fe/H]$ increasing from left to right; plus lines of constant age (dotted lines) have ages increasing from top to bottom in these grid plots. Therefore, this figure indicates that the ages in NGC 59 are consistent with ~ 2 to 6 Gyr, based on $H\beta$ as the main age indicator and slightly extrapolating to the left of the plotted grid (i.e. to lower $[Fe/H]$) for the centre and lower regions. For the upper region, which could be fitted with the EZ_AGES software, the following measurements were found: Age = $2.12^{+1.09}_{-0.45}$ Gyr; $[Fe/H] = -0.80^{+0.26}_{-0.24}$ dex; $[Mg/Fe] = -0.04^{+0.12}_{-0.09}$ dex.

Results for ages and $[Fe/H]$ from the MILES SSP fits are qualitatively consistent with those from EZ_AGES. For the upper region, the results from EZ_AGES are also quantitatively consistent within the estimated errors given in Table 4. One exception is that the best-fitting age from MILES fits to the lower region is very old. However, recall that we can only place a limit on this age as approximately > 8 Gyr, as discussed in Section 5.1 above. The good agreement between results from MILES SSP fits and EZ_AGES fits indicates that our SSP fitting results are not biased by the models used to fit the Lick indices.

5.3 New MILES data base – two burst models

We know that galaxies are not SSPs in reality, and that NGC 59 shows evidence of very recent star formation in the form of strong emission lines. Here we generate some predictions for two-burst SFHs, using the webtools and the latest version of SSPs from the MILES website (Vazdekis et al. 2010), at the MILES resolution (FWHM = 2.5 \AA). Composite spectra and Lick indices can be generated and downloaded.

We attempt a search of parameter space to see if the current data for NGC 59 are consistent with an old (~ 14 Gyr), metal-poor ($[Z/H] \sim -1.7$) burst plus a younger burst, whose age, metallicity and mass contribution we vary on a grid of models. Younger burst ages are from 0.063 to 1.0 Gyr, with possible metallicities of $[Z/H] = -1.7, -1.3, -0.7, -0.4, 0.0$ and mass contribution varied from 50 to 0.5 per cent. The rest of the mass is in the old SSP. These combinations were tested against the data for the centre region in NGC 59. The best fits are restricted by the fact that no interpolation of SSP models was available from the MILES website. A similar fit to that shown in Table 4 could be achieved, but only with the lowest

Table 4. SSP fits from MILES SSP templates at the Lick standard resolution. Note that $[Fe/H]$ is estimated from $[Z/H]$ and $[\alpha/Fe]$.

Region	Log(Age) (Gyr) (\pm)	$[Fe/H]$ (\pm)	$[\alpha/Fe]$ (\pm)	$[Z/H]$ (\pm)	No. ind.	Chi-sq reduced	Comment
Upper	0.550	-0.767	-0.300	-1.050	18	23.43	Emission-line region
	0.118	0.135	0.054	0.120			
Centre	0.700	-1.412	-0.120	-1.525	18	44.63	Stronger emission-line region
	0.047	0.211	0.177	0.089			
Lower	1.175	-1.405	-0.180	-1.575	17	26.64	Emission-line region; Fe5270 excluded
	0.082	0.236	0.192	0.122			

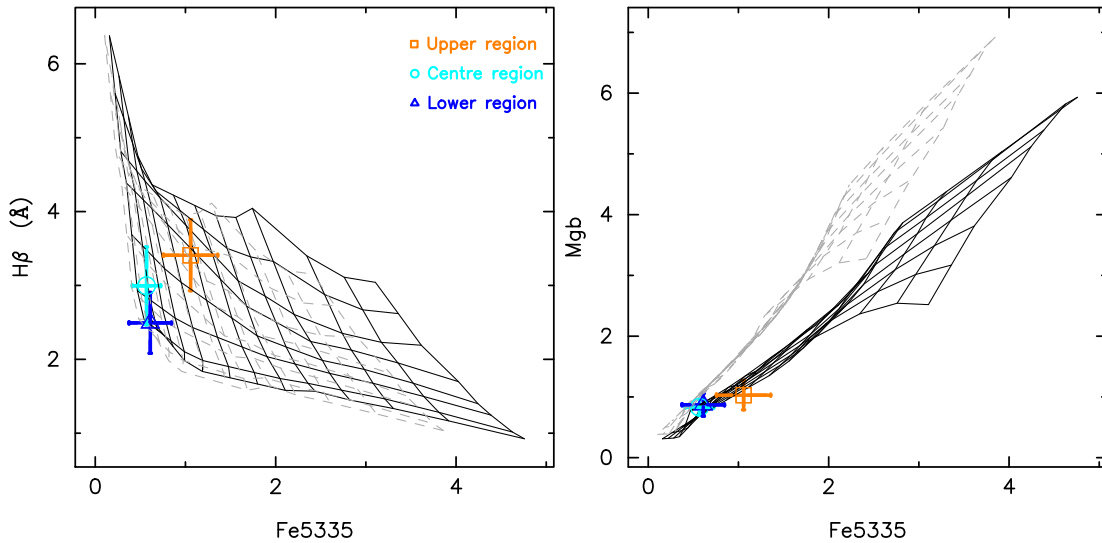


Figure 5. Index results for NGC 59, plotted against grids from MILES SSPs. The black grid is for $[\alpha/\text{Fe}] = 0$, while the grey grid is for $[\alpha/\text{Fe}] = +0.3$. In the left-hand plot, the age indicator $H\beta$ is plotted, with age increasing downwards on the grid, for $\text{Log}(\text{Age}(\text{Gyr})) = 0.0, 0.15, 0.3, 0.475, 0.7, 0.9, 1.075, 1.175$. The metallicity indicator Fe5335 is plotted, with metallicity increasing from left to right, from $[Z/H] = -2.25$ to $+0.80$, in steps of 0.25 dex. Solar metallicity is the fourth line from the right. This plot of age versus metallicity-sensitive features shows the low metallicity and relatively young age in NGC 59, with the upper region (orange) being the youngest and the lower region being the oldest (dark blue). The centre of NGC 59 (cyan) is intermediate in age between the two outer regions. The right-hand plot, of Fe5335 versus Mgb, highlights the unenhanced $[\alpha/\text{Fe}]$ ratios in NGC 59.

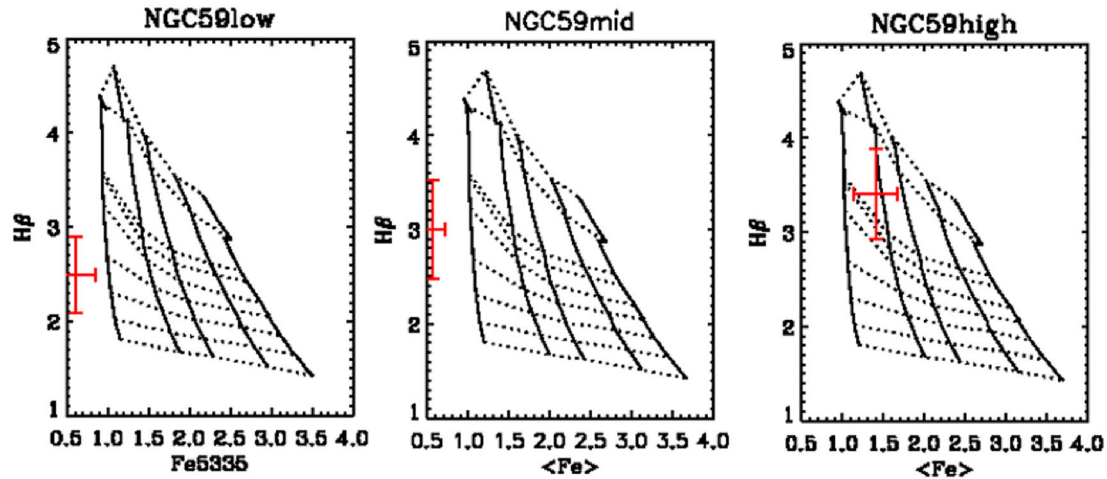


Figure 6. Grid plot showing results for NGC 59 from *EZ_AGES* fitting routine, for the three spatial regions across NGC 59. The Lick resolution data and errors are shown by the red plus sign. The upper region in NGC 59 (right-hand plot) can be fitted, with a metallicity lying within the range allowed by *EZ_AGES*. The lower and centre regions in NGC 59 (left-hand and middle plots) cannot be fitted, because of the low metal line strengths, indicating metallicities below those allowed for in *EZ_AGES* (i.e. $[\text{Fe}/\text{H}] < -1.3$). The age indicator ($H\beta$) is plotted on the vertical axes, whilst metallicity indicators are plotted on the horizontal axes ($\langle \text{Fe} \rangle = \text{Fe}5270 + \text{Fe}5335$ or Fe5335).

metallicity ($[Z/H] = -1.7$), and a small mass contribution (~ 1.5 per cent) from a young population (0.07 Gyr). This is equivalent to a frosting of young stars on an otherwise old, metal-poor stellar population. The fit became worse if a higher metallicity ($[Z/H] = -0.7$) was assumed for the old or young population. Therefore, only fits with low metallicity were possible, supporting the results from single SSP fitting that NGC 59 is a very low metallicity galaxy.

Attempting to fit more complex SFH, with intermediate age populations led to poorer fits, since intermediate age populations cannot reproduce weak enough metal-sensitive lines, at a given Balmer line strengths.

5.4 STARLIGHT full spectrum fits

Finally, as an additional check on the analysis, both for Balmer line processing and to check model fits, full spectrum fitting was attempted using *STARLIGHT* (Cid Fernandes et al. 2005). This was run with Bruzual & Charlot (2003) SSPs, for all the three apertures and with and without the cores of the strongest Balmer lines for each. Whether the Balmer lines were masked out or not, the results are very similar illustrating that our main results are not biased by the Balmer emission-line replacement process described in Section 3.3.

Also the *STARLIGHT* fits are broadly consistent with the results from fitting Lick indices. The mean light-weighted age is $\sim 3\text{--}4$ Gyr in all

three spectra. The STARLIGHT results show a widespread in the Gyr-scale population ages, with quite well-defined very young 5–20 Myr populations in addition which tend to dominate the *light* except in the upper aperture. The STARLIGHT fits indicate that less than 15 per cent of the light could come from populations younger than 25 Myr. Stellar mass is strongly dominated by the old population in all cases, with the oldest population in the lowest aperture similar to the Lick index results. Fitted mean metallicities are generally well below solar ($\sim 1/10$ th of solar) for both young and old populations, except for a young component contributing to the lower spectrum, which is closer to solar. With the input models used with STARLIGHT, we are not able to constrain abundance ratios in any way.

5.5 Discussion

The results illustrated in Fig. 5 do not change significantly when other indices combinations are selected, such as the higher order Balmer lines for ages, or the classic $[\text{Mg}<\text{Fe}>]$ combination used by many authors as an overall metallicity indicator. The left-hand plot in Fig. 5 illustrates why it is difficult to constrain ages in such low-metallicity systems as NGC 59, since the grid of models turns up to higher Balmer line strengths, for a given age. This is less apparent in the grid of models plotted in Fig. 6, since those models do not go down to such low metallicities. The right-hand panel in Fig. 5 illustrates the difficulty in measuring $[\alpha/\text{Fe}]$ accurately in such low metallicity systems, since the grids of SSP model predictions start to converge. This indicates how new measures of age and abundance patterns are needed in future, in order to understand the stellar population histories in these potential building block of luminous ETGs. There may be additional information in the bluer part of the spectrum, which is sensitive to abundance patterns (Sansom et al. 2013).

If low-mass ETGs formed the building blocks of higher mass ETGs through dissipationless mergers, then we might expect to see some relics of those building blocks still around today. They are predicted to have the high metallicity, high $[\alpha/\text{Fe}]$ ratios seen in luminous ETGs, if the build-up of galaxy mass is dissipationless. As yet, no such low-mass systems have been observed. The quasi-monolithic or early-hierarchical formation of ETGs easily accounts for enhanced $[\alpha/\text{Fe}]$ ratios in more massive galaxies, since there was not time for Fe enrichment from delayed SNIa to feed back into the stellar population. However, simultaneously generating the higher metallicities in such a scenario is difficult (e.g. Pipino et al. 2009, their fig. 8; Merlin et al. 2012, their fig. 13). In fact, NGC 59 has unusually low metallicity for its mass, making it an unlikely candidate for a dissipationless building block.

A mass–metallicity plot is shown in Fig. 7, with stellar velocity dispersion used as a proxy for mass, in which NGC 59 is contrasted with extrapolations from higher σ systems. The metallicity measured here for NGC 59 is well below such extrapolations. These data for NGC 59 also fall well below the $[\text{Fe}/\text{H}]$ central measurements for dE/dS0 galaxies in the sample of Koleva et al. (2011), their fig. 13, at similar σ , with NGC 59 being near the low end of their σ range. Koleva et al. (2011) found a range of, mostly negative, metallicity gradients in their dE/dS0 galaxies.

The above discussion is for metallicities of the stellar populations. The gas metallicity measured in NGC 59 is higher, typical of star-forming dwarf galaxies of this mass, as shown in Section 3.2. Systematic uncertainties in the emission-line strengths arising from uncertainties in the best-fitting stellar template were found to be negligible. Metallicities in H II gas associated with recent star formation will be higher than stellar abundances if the latest star formation is

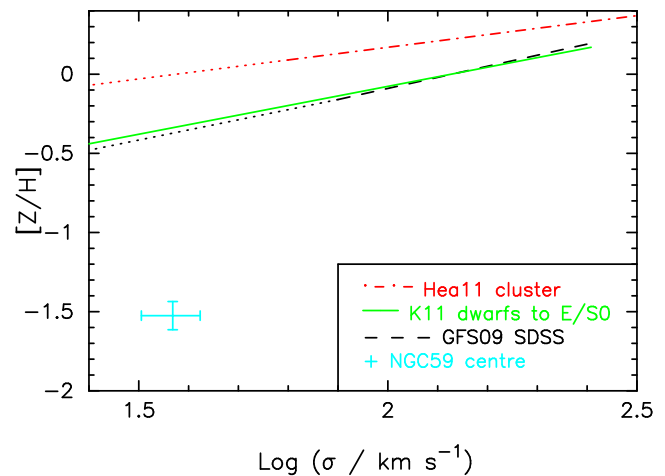


Figure 7. Plot showing $[\text{Z}/\text{H}]$ relation with $\text{Log}(\sigma)$, for samples of luminous ETGs, compared with results from the current observations for NGC 59. The mean trend from Graves et al. (2009, GFS09) is shown in black and from Harrison et al. (2011, Hea11) in red, with the current results for NGC 59 highlighted by a cyan cross. The trend shown from Koleva et al. (2011) in light green uses $[\text{Fe}/\text{H}]$ as a proxy for metallicity and includes both dwarf and giant ETGs. Solid lines show the range of $\text{Log}(\sigma)$ covered by the references and extrapolations to lower $\text{Log}(\sigma)$ are shown by dotted lines.

most metal enriched in a galaxy. However, the estimated gas metallicity in NGC 59 is significantly higher than the stellar metallicity. This may indicate that some or all of the gas was accreted from an enriched external source. Alternatively, simulations are needed to explore possible relationships between gas and star metallicities, for different SFHs, to see how different the gas and star metallicities can become.

More observations of statistically complete samples of lower mass ETGs are needed to probe their ranges of stellar population parameters and how the scaling relations behave at low masses. Such data will provide strong tests for hierarchical merger models of galaxy evolution (e.g. Kaviraj et al. 2009). Future large telescopes, such as the E-ELT, will be able to resolve stellar populations in galaxies at the distance of the Sculptor group, which will allow both an independent check on their stellar metallicities and measurements of their stellar metallicity distributions.

6 CONCLUSIONS

Scaling relations for ETGs rely on accurate data down to low luminosities (e.g. the Fundamental Plane, or the mass–metallicity relation discussed above). In this paper, we looked at one such low-luminosity ETG with data from the SALT, covering a broad wavelength range. These data stretch further into the blue region of the spectrum than most previous such studies, allowing for potentially stronger constraints on parameters such as stellar population age and abundance pattern (e.g. see Conroy et al. 2014). We also looked across the centre of the system to see how the bulk of the stellar population behaves.

Our main findings are that the low-luminosity ETG, NGC 59, has a young (SSP age ~ 2 to 6 Gyr), metal-poor (SSP $[\text{Fe}/\text{H}] \sim -1.4$ to -0.8) population near its centre, with evidence of an older underlying population ($> \sim 8$ Gyr) which is also very metal poor. The $[\alpha/\text{Fe}]$ ratio is difficult to accurately constrain with these data, for such a low-metallicity galaxy; however, all measurements are consistent with slightly subsolar values. Using two different sets of models led to similar results for the SSP parameters estimated from

Lick line strengths. These results are qualitatively in agreement with our previous results for NGC 59, but the measured metallicity is even lower than previously estimated. These data highlight the difficulty of measuring accurate ages for metal-poor systems, older than about 8 Gyr.

Fitting two-burst SSP models gave a better representation of the overall spectrum and NGC 59 was best fitted with an old (14 Gyr), metal-poor SSP plus a 1.5 per cent mass frosting of young (0.07 Gyr), metal-poor stars. Fits using *STARLIGHT* led to qualitatively similar results, confirming the low stellar metallicity in NGC 59, although no abundance pattern constraints are yet possible with these full spectrum fitting methods. We note that the gas-phase metallicity in the H II region close to the nucleus of NGC 59 is higher, $[O/H] \sim -0.7$, possibly suggesting external gas accretion of unknown origin. Results such as the ones shown here for NGC 59 and for larger samples of LLEs will be useful in future to constrain cosmological simulations and test hierarchical merging models of galaxy evolution and morphological transformations.

ACKNOWLEDGEMENTS

All of the observations reported in this paper were obtained with the SALT. The proposal code was 2012-1-UKSC-003, and the PI was Sansom. Thanks goes to the SALT support scientists for their help with these observations. PV and AYK acknowledge support from the National Research Foundation of South Africa. An RAS grant was awarded for an internship student, M.A. Deakin, to work on these data, plus a UCLan internship for J.J. Thirlwall. This research has made use of the SIMBAD database, operated at CDS, Strasbourg, France. This research has made use of the NASA/IPAC Extragalactic Database (NED), which is operated by the Jet Propulsion Laboratory, California Institute of Technology, under contract with the National Aeronautics and Space Administration. Thanks to R. Proctor for the use of his SSP fitting software and to M. Sarzi for help with *pPXF* and *gandalf* software. We thank V.P. Debattista and the anonymous referee for helpful comments that improved the paper.

REFERENCES

Abazajian K. et al., 2005, *AJ*, 129, 1755
 Annibali F., Grutzbach R., Rampazzo R., Bressan A., Zeilinger W. W., 2011, *A&A*, 528, A19
 Baldwin J. A., Phillips M. M., Terlevich R., 1981, *PASP*, 93, 5
 Beaulieu S. F., Freeman K. C., Carignan C., Lockman F. J., Jerjen H., 2006, *AJ*, 131, 325
 Bender R., Burstein D., Faber S. M., 1993, *ApJ*, 411, 153
 Bouchard A., Jerjen H., Da Costa G. S., Ott J., 2005, *AJ*, 130, 2058
 Bruzual G., Charlot S., 2003, *MNRAS*, 344, 1000
 Buckley D. et al., 2008, *Proc. SPIE*, 7014, 6
 Burgh E. B., Nordsieck K. H., Kobulnicky H. A., Williams T. B., O'Donoghue D., Smith M. P., Percival J. W., 2003, *Proc. SPIE*, 4841, 1463
 Calzetti D., Armus L., Bohlin R. C., Kinney A. L., Koornneef J., Storchi-Bergmann T., 2000, *ApJ*, 533, 682
 Cappellari M., Emsellem E., 2004, *PASP*, 116, 138
 Cid Fernandes R., Mateus A., Sodré L., Stasińska G., Gomes J. M., 2005, *MNRAS*, 358, 363
 Conroy C., Graves G. J., van Dokkum P. G., 2014, *ApJ*, 780, 33
 Crawford S. M. et al., 2010, *Proc. SPIE*, 7737, 773725
 de Swardt B., Kraan-Korteweg R. C., Jerjen H., 2010, *MNRAS*, 407, 955
 de Vaucouleurs G., de Vaucouleurs A., Corwin H. G., Jr, Buta R. J., Paturel G., Fouqu P., 1991, *Third Reference Catalogue of Bright Galaxies*. Springer, Berlin (RC3)

Falcón-Barroso J., Sánchez-Blázquez P., Vazdekis A., Ricciardelli E., Cardiel N., Cenarro A. J., Gorgas J., Peletier R. F., 2011, *A&A*, 532, 95
 Foster C. et al., 2012, *A&A*, 547, 79
 Gallazzi A., Charlot S., Brinchmann J., White S. D. M., 2006, *MNRAS*, 370, 1106
 Graves G. J., Schiavon R., 2008, *ApJS*, 177, 446
 Graves G. J., Faber S. M., Schiavon R. P., 2009, *ApJ*, 693, 486
 Grevesse N., Sauval A. J., 1998, *Space Sci. Rev.*, 85, 161
 Harrison C. D., Colless M., Kuntschner H., Couch W. J., de Propris R., Pracy M. B., 2011, *MNRAS*, 413, 1036
 Izotov Y. I., Thuan T. X., 1999, *ApJ*, 511, 639
 Izotov Y. I., Thuan T. X., Lipovetsky V. A., 1994, *ApJ*, 435, 647
 Izotov Y. I., Stasińska G., Meynet G., Guseva N. G., Thuan T. X., 2006, *A&A*, 448, 955
 Jerjen H., Binggeli B., Freeman K. C., 2000, *AJ*, 119, 593
 Johansson J., Thomas D., Maraston C., 2012, *MNRAS*, 421, 1908
 Karachentsev I. D., Kaisina E. I., 2013, *AJ*, 146, 46
 Kaviraj S., Rey S.-C., Rich R. M., Yoon S.-J., Yi S. K., 2007, *MNRAS*, 381, L74
 Kaviraj S., Devriendt J. E. G., Ferreras I., Yi S. K., Silk J., 2009, *A&A*, 503, 445
 Kelvin L. S. et al., 2014, *MNRAS*, 444, 1647
 Kniazev A. Y., Pustilnik S. A., Grebel E. K., Lee H., Pramskij A. G., 2004, *ApJS*, 153, 429
 Kniazev A. Y., Grebel E. K., Pustilnik S. A., Pramskij A. G., Zucker D., 2005, *AJ*, 130, 1558
 Kniazev A. Y. et al., 2008, *MNRAS*, 388, 1667
 Koleva M., Prugniel P., De Rijcke S., Zelinger W., 2011, *MNRAS*, 417, 1643
 Koleva M., Bouchard A., Prugniel P., De Rijcke S., Vauglin I., 2013, *MNRAS*, 428, 2949
 Korn A. J., Maraston C., Thomas D., 2005, *A&A*, 438, 685
 Loveday J., 1996, *MNRAS*, 278, 1025
 Merlin E., Chiosi C., Piovani L., Grassi T., Buonomo U., Barbera F. La., 2012, *MNRAS*, 427, 1530
 O'Donoghue D. et al., 2006, *MNRAS*, 372, 151
 Pipino A., Devriendt J. E. G., Thomas D., Silk J., Kaviraj S., 2009, *A&A*, 505, 1075
 Proctor R. N., Sansom A. E., 2002, *MNRAS*, 333, 517
 Recchi S., Calura F., Kroupa P., 2009, *A&A*, 499, 711
 Reines A. E., Nidever D. L., Whelan D. G., Johnson K. E., 2010, *ApJ*, 708, 26
 Rose J. A., Bower R. G., Caldwell N., Ellis R. S., Sharples R. M., Teague P., 1994, *AJ*, 108, 2054
 Sansom A. E., Northeast M. S., 2008, *MNRAS*, 387, 331
 Sansom A. E., Milone A. C., Vazdekis A., Sánchez-Blázquez P., 2013, *MNRAS*, 435, 952
 Sarzi M. et al., 2006, *MNRAS*, 366, 1151
 Saviane I., Ivanov V. D., Held E. V., Alloin D., Rich R. M., Bresolin F., Rizzi L., 2008, *A&A*, 487, 901
 Schiavon R. P., 2007, *ApJS*, 171, 146
 Schlegel D., Finkbeiner D., Davis M., 1998, *ApJ*, 500, 525
 Skillman E. D., Televis R. J., Kennicutt R. C., Jr, Garnett D. R., Terlevich E., 1994, *ApJ*, 431, 172
 Skillman E. D., Côté S., Miller B. W., 2003, *AJ*, 125, 593
 Thomas D., Maraston C., Bender R., Mendes de Oliveira C., 2005, *ApJ*, 621, 673
 Tolstoy E., Hill V., Tosi M., 2009, *ARA&A*, 47, 371
 Vazdekis A., Sánchez-Blázquez P., Falcón-Barroso J., Cenarro A. J., Beasley M. A., Cardiel N., Gorgas J., Peletier R. F., 2010, *MNRAS*, 404, 1639
 Venn K. A., Irwin M., Shetrone M. D., Tout C. A., Hill V., Tolstoy E., 2004, *AJ*, 238, 177
 Worthey G., 1994, *ApJS*, 95, 107
 Worthey G., 1998, *PASP*, 110, 888
 Worthey G., Ottaviani D. L., 1997, *ApJS*, 111, 377

This paper has been typeset from a $\text{\TeX}/\text{\LaTeX}$ file prepared by the author.